Abbreviations:

MK – Metakaolin; MIP – Mercury intrusion porosimetry; BET – Brunauer-Emmett-Teller; LOI – Loss on ignition; UPV – Ultrasonic pulse velocity; EPMA – Electron probe microanalysis; ICP-AES – Inductively coupled plasma emission spectroscopy.

Effect of alkali activators on diffusivity of metakaolin-based geopolymers

Kiyofumi Kurumisawa [a], Hiroaki Omatu [b] and Yuta Yamashina [c]

[a] Associate Professor, Faculty of Engineering, Hokkaido University, Kita 13 Nishi 8, Sapporo Hokkaido 0608628, Japan. kurumi@eng.hokudai.ac.jp.

[b] Graduated student, Graduated School of Engineering, Hokkaido University, Kita 13 Nishi 8, Sapporo Hokkaido 0608628, Japan. a9420376h@gmail.com.

[c] Undergraduate student, School of Engineering, Hokkaido University, Kita 13 Nishi 8, Sapporo Hokkaido 0608628, Japan. yutayamashina0520@gmail.com.

Correspondence: Kiyofumi Kurumisawa; Email: kurumi@eng.hokudai.ac.jp; Tel: +81-11-706-6319.

Abstract

A basic investigation into whether a geopolymer can be utilized as a part of an artificial barrier during radioactive waste disposal was conducted in this study. Geopolymers are comprised primarily alumina and silica, and they exhibit negligible leaching owing to the absence of calcium. Studies on geopolymers are limited compared to those on other cementitious materials because the physical characteristics of geopolymers vary with the production conditions. In this work, metakaolin (MK)-based geopolymers were prepared, and their diffusion performance was analyzed. The results indicate that the diffusivity of cesium in a geopolymer is affected by the type of alkali activator. Sodium-activated geopolymers had higher cesium adsorption capacity than potassium-activated geopolymers. The cesium adsorption capacity also had a significant effect on the diffusivity of cesium in the geopolymers. It was shown that,

in addition to the pore structure and surface area, the mobility of water affects the diffusion performance of the geopolymer.

Keywords: Geopolymer, Metakaolin, Diffusion, Adsorption, Pore structure

1. Introduction

The disposal of radioactive waste from nuclear power plants is a significant challenge in Japan. The development of technologies for decommissioning nuclear facilities has become a critical issue following the accident at the Fukushima Daiichi Nuclear Power Station that produced a substantial quantity of radioactive waste. There is ongoing research to reduce the volume of radioactive waste and to develop suitable disposal techniques. Methods of radioactive waste disposal may be divided into four categories, depending on the radiation level of the waste: trench disposal, pit disposal, medium-depth disposal, and geological disposal. Effective disposal of radioactive waste is achieved using multiple protective barriers, both artificial and natural, to suppress the migration of radionuclides. These barriers delay the diffusion and migration of radionuclides, thereby inhibiting interactions between the waste and the living environment. For safety, radioactive materials must be confined until their effects are minimized; thereafter, the level of supervision can be relaxed one step at a time. The capacity of artificial barrier materials to confine radionuclides is determined by evaluating the radioactive concentration and characteristics of the waste. It is expected that cement-based materials, such as concrete, can be used as artificial barriers in deep-depth disposal facilities. However, elution of the calcium component of calcium silicate hydrate (C-S-H) may induce porosity in cement-based materials.

It has been demonstrated that leaching induces variations in the diffusion performance of cementitious materials [1]. Leaching-induced variations in the diffusion coefficient are attributed to the elution of calcium hydroxide from hardened cement. However, the diffusion coefficient may increase in blended cements that contain fly ash and blast furnace slag powders. This study conducts a basic investigation into whether geopolymers can be utilized as a part of an artificial barrier during radioactive waste disposal. Joseph Davidovits, a French scientist, proposed the term "geopolymer" in 1988 to describe solids formed by the reaction between active fillers and alkaline solutions [2]. Initially, geopolymers attracted significant attention because they are fire resistant, unlike the flammable organic polymers. Geopolymers are utilized in civil engineering and construction, and as a solidifying material for industrial and radioactive waste [2]. They can be produced by the reaction of blast furnace slag or fly ash, an industrial by-product, with an alkaline solution. This polycondensation reaction is accompanied by dehydration, which results in significant shrinkage during curing, and high acid resistance. Alkali-aggregate reactions are negligible in geopolymer systems; furthermore, the fire resistance of geopolymers is superior to that of ordinary Portland cement. The reaction between blast furnace slag and an alkaline solution yields C-S-H, which is an alkali-activated slag (AAS), not a geopolymer [3]. The alkaline aluminosilicate structure of geopolymers is similar to that of natural zeolite. This structure consists of aluminum and silicon connected in the form of three-dimensional tetrahedra. Hardened geopolymers exhibit low CO_2 emissions during cement production, as well as high leaching resistance [2,4]. However, the physical properties of these materials vary depending on the materials used for synthesis. The rheological properties depend on the alkali [4, 5], and the reactivity depends on the types of metakaolin (MK) and alkali. The strength development varies depending on the amount of Si added to the alkali activator [6–9]. The reported Si/Al ratio used to optimize the strength development varies between studies. The optimal curing temperature was reported to be 40 °C in one study [10] and 60 °C in others [11–13]. It has been reported that the fluidity and strength development vary depending on the types of MK and alkaline solution used for synthesis [14–17]. There has been extensive research on the diffusion performance of geopolymers and alkali activated materials manufactured using blast furnace slag and fly ash [18–24]. In addition, the elution of Cs and Sr from zeolite embedded in geopolymers has been investigated [21, 25, 26]. Although many studies have been conducted on the immobilization

of heavy metals with respect to metakaolin geopolymers[27, 28], there are few papers on the penetration of ion from the outside[29–32]. In the above-mentioned previous studies, only the results of using sodium-type activators were used, and no experiments were conducted in which potassium-type activators or changes in Si/Al of activator were performed. Despite multiple studies on the diffusivity of chloride ions, the diffusivity of cations in MK-based geopolymers remains relatively unexplored. It is necessary to understand the diffusion performance to predict the durability of MK-based geopolymer structures because some radionuclides also contain cations (Sr^{2+}, Cs^{+}). Moreover, few studies have explored the relationship between the pore structure, the state of the water, and the diffusion performance of the geopolymer. In this study, the effect of the type of alkaline activator on the diffusivity of Cs is elucidated. Variations in the pore structure are investigated using mercury intrusion porosimetry (MIP) and nitrogen adsorption measurements. Furthermore, low temperature differential scanning calorimetry (LT-DSC) measurements and proton nuclear magnetic resonance (NMR) measurements are used to analyze the state of water in geopolymer samples.

2. Material and methods

2.1. Materials used and specimen preparation

MK (Metamax, BASF), whose chemical composition is presented in Table 1, is an aluminosilicate powder that was utilized as a source of alumina and silica (SiO_2/Al_2O_3=2.0 in mol/mol). The average particle size and the Brunauer–Emmett–Teller (BET) specific surface area were 1.3 μm and 12.9 $m^2 \cdot g^{-1}$, respectively. According to the X-ray diffraction (XRD) measurements with an internal standard (corundum), as shown in Supplement Figure 1, most of the MK was amorphous. The alkali activators were prepared using potassium silicate solution (FUJIFILM Wako Pure Chemical Corporation), sodium

silicate solution (FUJIFILM Wako Pure Chemical Corporation), potassium hydroxide (KANTO CHEMICAL CO.,INC.), sodium hydroxide (KANTO CHEMICAL CO.,INC.) as reagent grade, and purified water that had conductivity of less than 0.1 mS/m. Alkali activators were mixed with chemicals at least 24 hours before geopolymer preparation. The compositions of the alkali activators are summarized in Table 2, where M_2O represents K_2O and Na_2O. The alkali activators were prepared based on the molar ratio of Al_2O_3 contained in the MK. The Si NMR results for the alkali activators are shown in Supplement Figure 2. The values of Q^0 (-71.6 ppm), Q^1(-79.1 ppm), Q^2(-81.4 and -87.2 ppm), and Q^3(-89.4 and -95.3 ppm) were assigned based on previous studies [8, 33, 34]. The symbol Q^{Δ} stands for cyclic oligomers, showing the same connectivity as Q^2 and Q^3 environments but with different bond angles. A sharp peak was observed with the sodium type activator, and a broad peak was observed with the potassium type activators in Q^0 and Q^1. Table 3 shows the results of deconvolution by the Dmfit software[35]. The amount of Q^2 and Q^3 was high in 0.66K, but Q^0 and Q^1 accounted for 50% of the other activators. Previous studies have reported the mixing proportions that have sufficient strength, and these were determined based on the requirements for investigations into the effects of the alkali cation (Na or K), Si/Al ratio, and water content (H_2O/Al_2O_3: 9.0 or 11.0 mol) [7, 36]. For example, in specimen K11, the composition of the geopolymer where MK has reacted completely was $K_2O{\cdot}3SiO_2{\cdot}Al_2O_3{\cdot}11H_2O$. The synthesized alkali activators were mixed with MK. For preparation of the mortar samples, the mass of sand was three times the mass of MK.

To produce the mortar, sand, MK, and alkali activator were mixed for 15 min using a mixer (speed: 198 rpm). First the sand and MK were mixed in a mechanical mixer for 30 seconds, after which the alkali activator was added and mixed. The mixture was placed in a predetermined mold. The air within the specimens was removed using a vibrator after mixing. The specimens were cured by sealing them with a polyethylene film to prevent evaporation, and aging them for up to 28 days at 23 °C. The mortar samples were used for the mechanical property tests, and the paste samples without sand were used for microstructural analysis. The preparation procedure of paste is the same as for mortar except for sand.

2.2. Measurement techniques

The physical characteristics of the specimens were determined via uniaxial compressive strength tests, ultrasonic pulse velocity (UPV) tests, diffusion coefficient measurements, and adsorption measurements. The pore structure was examined using MIP and the nitrogen adsorption method.

2.2.1. Moisture content and loss on ignition (LOI)

The samples were crushed to 5 mm or less by hammer, and dried at 105 °C. Thus, the moisture content (*mc*) was determined by measuring the change in the mass. The water content was calculated by the following formula.

$$mc = \frac{m_{20℃} - m_{105℃}}{m_{105℃}} \qquad (1)$$

Here, $m_{20℃}$ is the mass of sample at 20 ° C, and $m_{105℃}$ is the mass of sample at 105° C. However, a small amount of water can evaporate during crushing. The LOI of specimen was determined from the change in the mass of the samples between 105 and 950 °C.

$$LOI = \frac{m_{105℃} - m_{950℃}}{m_{950℃}} \qquad (2)$$

Here, $m_{950℃}$ is the mass of sample at 950 ° C.

2.2.2. Uniaxial compressive strength measurement

Cylindrical specimens (Φ 50 mm × 100 mm) were utilized for the compressive strength test. The uniaxial compressive strength was measured using an automatic compression tester. The maximum stress during the test, obtained from the breaking point of each specimen, was divided by the cross-

sectional area of the end face to calculate the uniaxial compressive strength. The test was repeated with three specimens for each activator, and the average value was taken as the compressive strength.

2.2.3. UPV measurement

Cylindrical specimens (Φ 50 mm × 100 mm) were utilized for the UPV measurement. Grease was applied to the end face of each test piece, and the ultrasonic propagation time was measured. The ultrasonic propagation velocity was calculated by dividing the length of the specimen by the measured time. The test was repeated with three specimens for each activator, and the average value was taken as the UPV.

2.2.4. Diffusion coefficient measurement

Cylindrical specimens (Φ 50 mm × 50 mm) were utilized for the diffusion test. One side of each specimen was exposed, while the other side was covered with epoxy resin. The specimens were immersed in a 50 mM solution of cesium chloride for 1 week or 4 weeks. The cross section of each specimen was dry-polished and subjected to electron probe microanalysis (EPMA: JXA-8530F, JEOL) to determine the distribution of cesium and chloride after immersion. The conditions of EPMA were measured at an acceleration voltage of 15 keV and a sample current of 5 nA. The measurement interval for EPMA was 0.1 mm. The apparent diffusion coefficient of cesium (D_{ap}) was determined based on the assumption that the concentration distribution of cesium followed Fick's second law. This is given by

$$C(x,t) = C_i + C_0\left\{1 - erf\left(\frac{x}{2\sqrt{(D_{ap} \times t)}}\right)\right\} \qquad (3)$$

where C_i is the initial ion content in the material (mass %), C_0 is the ion content at the surface (mass %), *erf* is the error function, x is the distance from the surface (m), and t is the immersion time (s).

2.2.5. Adsorption measurement

Once the geopolymer reached the specified age, it was roughly crushed with a hammer to 2.5–5 mm particles. Then, 5 g samples were immersed in 100 ml of 1, 2, 4, 8, 10, and 20 mM cesium chloride solutions for 4 weeks. Subsequently, the concentration of each element in the solution was measured using inductively coupled plasma-atomic emission spectroscopy (ICP-AES; CIROS CCD, Spectro Analytical Instruments GmbH, Kleve, Germany). Thereafter, the solution was diluted 10-fold and subjected to the analysis. The saturated adsorption amount was determined by considering Langmuir-type adsorption using the equation [21]:

$$Q_e = \frac{QbC_e}{1 + bC_e} \qquad (4)$$

where Q_e is the equilibrium sorption amount of cesium ions on the adsorbent (mmol g^{-1}), C_e is the equilibrium concentration of cesium ions (mmol L^{-1}), Q is the monolayer adsorption capacity (mmol g^{-1}), and b is the constant that is related to the free energy of adsorption.

2.2.6. Pore structure analysis

Once the geopolymer paste reached the specified age, it was roughly crushed with a hammer to 2.5–5 mm particles. The reaction was stopped using liquid nitrogen and a freeze dryer. Subsequently, the pore

size distribution was determined by MIP (AutoPore V 9620, Micromeritics Instrument Corporation, Georgia, USA). The measurement range of the pore size was 3–400 μm. A 0.5 g sample was used for the measurement.

The sample was crushed in a ball mill, and the powder was utilized for the BET adsorption analysis. Vacuum drying was performed at room temperature for 24 h. The specific surface area and pore structure of the sample were determined using nitrogen adsorption measurements (BELSORP Max, MicrotracBEL Corporation, Osaka, Japan). The sample was approximately 0.2 g, and the BET specific surface area was calculated from the nitrogen adsorption measurements.

2.2.7. Solid state NMR

Solid-state NMR was used to analyze the chemical bond state of silica and aluminum in the geopolymer. The powdered sample was used for ^{29}Si DD MAS NMR and ^{27}Al MAS NMR measurements (AVANCE III 600WB, Bruker). The observed frequencies were 119.26 and 156.41 MHz, respectively; the spinning speed was 12 kHz; and the waiting times were 20 and 5 seconds, respectively. In addition, liquid ^{29}Si DD NMR measurements of the alkali activators were made; the relaxation time was 2.0 s, and the total scanning number was 5632. For the liquid NMR measurements, 10 mass% of deuterium water was added to the alkali activators.

2.2.8. Proton NMR measurement

Proton NMR (minispec, Bruker) was used to examine the state of the water in the paste samples (8 mm in diameter). The paste sample was placed in a glass tube and measured. Proton NMR measures the presence of water contained inside the specimen by nuclear magnetic resonance, and the shorter the relaxation time of proton, the more the state of water is affected and constrained by the solid surface. For the ^{1}H NMR measurement, the Car–Purcell–Meiboom–Gill (CPMG) method was applied, and the relaxation time T2 was recorded. The CPMG method mainly facilitates measurements of protons in a

liquid state [38]. For this measurement, 0.47 T NMR apparatus was used. The experiment used a 2.5 μs pulse at 90°, and a 5.0 μs pulse at 180°, with a pulse interval ($90° \leq \tau \leq 180°$) of 40 μs. The number of recorded echoes in the CPMG echo train was 256, the time between observation points was 85 μs, the number of scans was 32, and the waiting time between repetitions was 5 s. In addition, a preliminary study confirmed that the number of integrations yielded a sufficient signal/noise ratio for analysis. In some previous studies, measurements were performed by changing τ [38, 39], but preliminary tests confirmed that the results obtained using a single τ did not differ. It has also been reported that the presence of aluminum affects the signal, but the measurements herein were performed to observe the qualitative effect [40].

2.2.9. LT-DSC measurement

LT-DSC measurements were used to identify the state of the water in the paste samples. In the LT-DSC results, the smaller the pores of water, the lower the freezing temperature. The paste samples were placed in a stainless pan (15 μL), which was then inserted into a low temperature differential scanning calorimeter (DSC6220, SII). The samples had an approximate mass of 60 mg, and 25 mg of α-Al_2O_3 powder was used as a reference sample. Each sample was exposed to a single measurement cycle wherein the temperature changed from 10 °C to -65 °C and back to 10 °C at a rate of 1.0 °C/min. The minimum temperature of -65 °C was used for heat exchange because the water/ice phase change has not been observed at lower temperatures [41].

2.2.10. Scanning electron microscopy (SEM) and energy dispersive X-ray (EDX) analysis

SEM (JSM-IT200, JEOL) was used to characterize the microstructure of the samples. In the SEM observations, the crushed samples were embedded in epoxy resin, and a cross-section with a polished surface was observed. Platinum sputtering was used to make the surface electrically conductive. The

procedure was performed at an accelerating voltage of 15 keV and a working distance of 10 mm. In addition, EDX point analysis was used to determine the elemental composition of the product in the geopolymers. In the point analysis, 10 or more points were analyzed using the ZAF method, and the average value was calculated.

3. RESULTS AND DISCUSSION

3.1. Uniaxial compressive strength and UPV measurements

Figure 1 shows the results of the compressive strength tests and UPV measurements. The 0.66K sample had the highest compressive strength (59MPa), and the K9 sample had the highest UPV (4km/s). A sample with a Si/Al ratio of approximately 2.0 has previously been reported to have the highest compressive strength [7]. Therefore, the 0.66K sample in this study exhibited the highest compressive strength. The K9 sample exhibited a high UPV owing to its low moisture content (Supplement Figure 3). The compressive strength and UPV of the sodium-based sample, N11, were 25% higher than those of the potassium-based sample, K11. This is because sodium induced the formation of a strong matrix [7]. The KN11 sample was weakest, and the reason for this will be explained in Section 3.4. Regarding the difference between the UPV and compressive strength results, it is considered that the air remaining in the highly viscous sample such as K9 and N11 at the fresh state affected the compressive strength.

3.2. Diffusion coefficient measurement

The cesium distribution in the geopolymers was determined by EPMA, and it is presented in Supplement Figure 4. The cesium penetration depth in the K11 sample was greater than that in the K9 sample. The EPMA did not detect chlorine in the specimen. The molecular dynamics calculations

suggest that chloride ions were repulsed by the N-A-S-H surface [42]. Therefore, the diffusion coefficient of chlorine was not obtained in this study. Figure 2 presents the apparent diffusion coefficients of cesium ions in the geopolymers. The diffusion coefficient of chloride ions in a slag-based geopolymer is approximately 10^{-13} $m^2 \cdot s^{-1}$ [22, 23], which is approximately identical to the diffusion coefficient of cesium in the MK-based geopolymers. The diffusion coefficients of the specimens immersed for one week were 10-70% higher than those immersed for four weeks, which is consistent with the results for the cementitious samples [43, 44]. This can be attributed to the blockage of pores owing to the penetration of cesium; however, further studies are required to confirm this. The K9 sample presented a low diffusion coefficient because the diffusion of cesium was suppressed by the low moisture content. The N11 sample also presented a low diffusion coefficient, and the diffusion coefficient of the KN11 sample was intermediate between those of the N11 and K11 samples. This indicates that sodium reduced the diffusion coefficient of cesium in the geopolymers. Comparing the diffusion coefficients of the K11 and 0.66K samples revealed that differences in the Si/Al ratios of the geopolymers had a negligible effect on them.

3.3. Adsorption measurement

The cesium adsorption isotherms are presented in Fig. 3a. The adsorption measurements were also performed for chlorine, but there was no change in the concentration of the solution, and no adsorption occurred. The amount of adsorbed cesium in the sodium-activated geopolymers was approximately 10% higher in the high-concentration regions. It has been reported that cesium is also adsorbed by fly ash-silica fume blend geopolymers [37]. The adsorption of cesium was characterized as Langmuir-type adsorption (Equation (4)), and the calculated monolayer adsorption capacities are presented in Fig. 3b. These results confirm the high adsorption capacities of sodium-activated geopolymers. The adsorption capacities of the sodium-activated geopolymers in this study were 3% higher than those in the previous study [37].

Figure 4 shows a plot of the adsorption capacities and apparent diffusion coefficients of the different samples. The diffusion coefficient tended to decrease as the adsorption capacity increased, but no strong correlation was found. Therefore, the amount of adsorption is an important factor for controlling diffusion performance, but other factors also affect the diffusion performance of geopolymers.

3.4. Pore structure analysis

The porosities and BET specific surface areas of the geopolymers were determined by MIP and nitrogen adsorption measurements, respectively. The results are presented in Fig. 5. The 0.66K sample had the lowest porosity(0.15mL/g), followed by the K9 sample(0.2mL/g). The results of the porosity measurements were similar to those of the moisture content measurements (Supplement Figure 3). The 0.66K sample had the highest specific surface area, and the specific surface areas of the potassium-activated geopolymer (K11) were 3 times higher than those of the sodium-activated geopolymer (N11). This is because the potassium-activated geopolymers were polymerized to a greater extent than the sodium-activated geopolymers; moreover, the potassium-activated geopolymers possessed densified microstructures. Figure 6 shows the pore size distribution of the geopolymers, as determined by MIP. The pore diameter peaks for sodium- and potassium-activated geopolymers were approximately 10 and 4 nm, respectively. This is indicative of the dense structure of the potassium-activated geopolymers, and the results are consistent with those obtained from the specific surface area measurements (Fig. 5).

A correlation was established between the compressive strengths and porosities of the geopolymers, as shown in Fig. 7a. The compressive strength increased as the porosity decreased as shown in previous studies[45, 46]. Therefore, the KN11 sample showed the lowest compressive strength, and the 0.66K sample showed the highest strength. However, no correlation was established between the diffusion coefficients and porosities of the geopolymers, as shown in Fig. 7b. Generally, the diffusion coefficient increases with the porosity of the material[19]. Sample K9 exhibited a low diffusion coefficient owing to its low porosity. Figure 7c shows a plot of the BET surface area and diffusion coefficients of the

geopolymers. A good correlation was found between them, and the diffusion coefficient increased as the BET surface area increased. This is considered to be due to the larger the surface area, as the larger the contact area with the ions promotes ion exchange for the cations in the geopolymer, which makes it easier for the cesium ions to diffuse. As shown in 3.3, it is considered that cesium ions that could not be adsorbed due to the low adsorption capacity of the potassium-type geopolymer diffuse inside.

3.5. Solid state NMR and SEM-EDX analysis

Figure 8a and 8b show the ^{27}Al NMR results and the ^{29}Si NMR results, respectively. The NMR results for ^{27}Al indicated that all the specimens formed a 5-coordinated structure, because the peak position was approximately 59 ppm. In the ^{29}Si NMR results, 0.66K sample can be considered as having a structure in which Al is bi-coordinated to Si, and the other samples have a structure in which Al is 3-coordinated [47]. This is because the chemical state of Si in the alkaline activator is different as shown in Table 3. However, the solid-state NMR results show that there was no significant difference in the skeletal structure within the solids of the geopolymers.

Some unreacted MK was present in the N11 sample, but none was observed in the other samples (Supplement Figure 4). It has been reported that this reaction is delayed owing to the high viscosity of sodium silicate solution [9]. The EDX measurement results (Supplement Table 1) confirm that the composition depends on the proportions of the mixture. Therefore, the reaction is considered to have been sufficiently close to completion.

3.6. State of water measured via LT-DSC and Proton NMR

Figures 9a and 9b show the results of the LT-DSC freezing and melting processes, respectively. The water in the pores froze at the temperature where the peak occurred during the freezing process, and the ice melted during the melting process. The lower the temperature, the more water in the small pores was frozen or thawed by the theory of thermoporometry [48]. In the K11 and KN11 specimens, the peak at approximately -20 °C was large, suggesting that there were many large pores [49]. In the 0.66K

sample, many small pores were present, indicated by many peaks below -30 °C. The total amount of heat detected was relatively small in the K9 and N11 samples; this indicates that little water was present in the pores of these specimens. The amount of water frozen to -30 ° C in the K11 specimen was more than 10 times higher than that in the N11 sample, the total amount of water in K9 and N11 was half that of the K11 sample. The total amount of frozen water was in the order of K11 > KN11>0.66K > K9 > N11. This order is the same as the order of the diffusion coefficient of the geopolymer. Therefore, since the amount of water that can be frozen in the N11 sample is small, it was shown that the water inside the pores is greatly affected by the solid surface, which suppresses mass transfer. These results differed from the MIP results; this is considered to be due to structural changes caused by drying the samples. During the melting process, a large peak was detected at approximately 0 °C for all the samples as shown in Fig.9b. Hysteresis may have occurred during the freezing and melting processes due to cracks appearing in the specimens during measurement, but the details are currently unknown and should be investigated in future.

Figure 10a shows the proton NMR measurement results. The signal intensity is proportional to the quantity of protons detected in the specimen. The initial signal intensity decreased in the order of K11 > 0.66K > K9 > KN11 > N11, indicating that they contained different amounts of free water, as shown in Supplement Fig. 3. This was in good agreement with the LT-DSC results except for KN11. It was shown that the relaxation of protons in the pores of the K11 and 0.66K samples was slow, and that it was fast in the pores of the N11 sample. Figure 10b shows the normalized signal intensity results obtained by dividing the observed signal intensity by the initial signal intensity. When the effect of the initial value is excluded, the proton relaxation is notably faster in the sample containing sodium. The time it takes for the signal intensity of the N11 specimen to decay in half is 1.76 times faster than that of the K11 and 0.66K specimens. This result also shows that the pore water of the N11 specimen is strongly constrained to the solid surface, which is considered to be the result of suppressing the diffusion of ions.

From the results of the two measurement methods, the sample containing sodium was more strongly influenced by the water near surface of solid than the sample containing only potassium, which resulted

in water being confined to the pores and the movement of ions being suppressed. Furthermore, the viscosity of the pore solution in the potassium-activated geopolymers was lower than that in the sodium-activated geopolymers, which facilitated the transfer of substances. It has been shown that the alkali activator of sodium is highly viscous with respect to the fluidity of the geopolymer paste [50]. Therefore, it was clarified that it is effective to use a sodium-type alkali activator to suppress the diffusion of cations. Moreover, research has been conducted, using different materials, which has shown that the durability of cement concrete can be increased by changing the viscosity of the pore solution[51]. On the other hand, even in a potassium-type specimen such as the K9 specimen, it is possible to suppress the diffusion of ions by reducing the amount of water in the activator. When considering the diffusion of ions in the geopolymer, it is necessary to clarify not only the porosity but also the state of pore water in the geopolymer.

4. CONCLUSIONS

This study demonstrated the diffusivity of cesium in MK-based geopolymers. The following conclusions were obtained from the investigations:

1. The use of sodium-based alkali activators and a decrease in the moisture content of the alkali activators lowered the apparent diffusion coefficients of cesium in MK-based geopolymers. The diffusion of chlorine could not be confirmed for the MK-based geopolymers in this study.
2. The use of sodium-based alkali activators increased the cesium adsorption capacities of MK-based geopolymers, and the adsorption of cesium was characterized as Langmuir-type adsorption. However, the adsorption of chlorine by the geopolymers could not be confirmed in this study.
3. A correlation between the compressive strength and porosities of MK-based geopolymers was established. Although no clear correlation between the diffusion coefficients and porosities of

MK-based geopolymers was identified, there was good correlation between the BET surface area and diffusion coefficient of cesium in MK-based geopolymers. Therefore, it was shown that the surface area is the main factors controlling the diffusion performance of MK-based geopolymers. It is recommended to use a sodium-type activator to suppress the diffusion of cesium ions in the geopolymer, or to reduce the amount of water in the potassium-type activator as well.

4. The LT-DSC and proton NMR results showed differences due to the state of water in the pores. It was shown that the sample containing sodium was more strongly affected by the water near surface of solid than the sample containing only potassium, resulting in the confinement of water in pores and suppression of the movement of ions.

CREDIT AUTHORSHIP CONTRIBUTION STATEMENT

Kiyofumi Kurumisawa: Supervision, Conceptualization, Methodology, Writing- Original draft preparation, Writing- Editing. **Hiroaki Ohmatsu:** Methodology. **Yuta Yamashina:** Methodology.

DECLARATION OF COMPETING INTERESTS

The authors declare that they have no known competing financial interests or personal relationships that could have appeared to influence the work reported in this paper.

ACKNOWLEDGMENTS

This work was supported in part by the Ministry of Economy, Trade and Industry (METI). A part of this work was conducted at the Joint-use Facilities: Laboratory of Nano-Micro Material Analysis, Hokkaido University, supported by the "Nanotechnology Platform" program of the Ministry of Education, Culture, Sports, Science and Technology (MEXT), Japan. We express our gratitude to these sources.

REFERENCES

1. Kurumisawa K, Haga K, Hayashi D, Owada H (2016) Effects of calcium leaching on diffusion properties of hardened and altered cement pastes. Phys Chem Earth 99:175–183. https://doi.org/10.1016/j.pce.2017.03.007
2. Joseph Davidovits (2008) Geopolymer Chemistry and Applications
3. Provis JL (2018) Alkali-activated materials. Cem Concr Res 114:40–48. https://doi.org/10.1016/j.cemconres.2017.02.009
4. Duxson P, Fernández-Jiménez A, Provis JL, et al (2007) Geopolymer technology: the current state of the art. J Mater Sci 42:2917–2933. https://doi.org/10.1007/s10853-006-0637-z
5. Palacios M, Puertas F, Banfill PFG (2007) Rheological Behaviour of Alkali-Activated Slag Pastes and Mortars. Effect of Admixtures. 12th ICCC, Montr Canada 80
6. Gharzouni A, Joussein E, Samet B, et al (2015) Effect of the reactivity of alkaline solution and metakaolin on geopolymer formation. J Non Cryst Solids 410:127–134. https://doi.org/10.1016/j.jnoncrysol.2014.12.021

7. Duxson P, Mallicoat SW, Lukey GC, et al (2007) The effect of alkali and Si/Al ratio on the development of mechanical properties of metakaolin-based geopolymers. Colloids Surfaces A Physicochem Eng Asp 292:8–20. https://doi.org/10.1016/j.colsurfa.2006.05.044

8. Duxson P, Provis JL, Lukey GC, et al (2005) Understanding the relationship between geopolymer composition , microstructure and mechanical properties. 269:47–58. https://doi.org/10.1016/j.colsurfa.2005.06.060

9. Duxson P, Lukey GC, Separovic F, Deventer JSJ Van (2005) Effect of Alkali Cations on Aluminum Incorporation in Geopolymeric Gels. 832–839. https://doi.org/10.1021/ie0494216

10. Rovnaník P (2010) Effect of curing temperature on the development of hard structure of metakaolin-based geopolymer. Constr Build Mater 24:1176–1183. https://doi.org/10.1016/j.conbuildmat.2009.12.023

11. Muñiz-Villarreal MS, Manzano-Ramírez A, Sampieri-Bulbarela S, et al (2011) The effect of temperature on the geopolymerization process of a metakaolin-based geopolymer. Mater Lett 65:995–998. https://doi.org/10.1016/j.matlet.2010.12.049

12. Mo BH, Zhu H, Cui XM, et al (2014) Effect of curing temperature on geopolymerization of metakaolin-based geopolymers. Appl Clay Sci 99:144–148. https://doi.org/10.1016/j.clay.2014.06.024

13. Aredes FGM, Campos TMB, MacHado JPB, et al (2015) Effect of cure temperature on the formation of metakaolinite-based geopolymer. Ceram Int 41:7302–7311. https://doi.org/10.1016/j.ceramint.2015.02.022

14. Sasaki K, Kurumisawa K, Ibayashi K (2019) Effect of retarders on flow and strength development of alkali-activated fly ash/blast furnace slag composite. Constr Build Mater 216:337–346. https://doi.org/10.1016/j.conbuildmat.2019.05.022

15. Benavent V, Frizon F, Poulesquen A (2016) Effect of composition and aging on the porous structure of metakaolin-based geopolymers. J Appl Crystallogr 49:2116–2128. https://doi.org/10.1107/S1600576716014618

16. Pouhet R, Cyr M, Bucher R (2019) Influence of the initial water content in flash calcined metakaolin-based geopolymer. Constr Build Mater 201:421–429. https://doi.org/10.1016/j.conbuildmat.2018.12.201

17. Rouyer J, Benavent V, Frizon F, Poulesquen A (2017) Influence of geopolymer formulation parameters on the elastic and porous properties over a one-year monitoring. Mater Lett 207:121–124. https://doi.org/10.1016/j.matlet.2017.06.125

18. Tennakoon C, Shayan A, Sanjayan JG, Xu A (2017) Chloride ingress and steel corrosion in geopolymer concrete based on long term tests. Mater Des 116:287–299. https://doi.org/10.1016/j.matdes.2016.12.030

19. Yang T, Yao X, Zhang Z (2014) Quantification of chloride diffusion in fly ash-slag-based geopolymers by X-ray fluorescence (XRF). Constr Build Mater 69:109–115. https://doi.org/10.1016/j.conbuildmat.2014.07.031

20. Osio-Norgaard J, Gevaudan JP, Srubar W V. (2018) A review of chloride transport in alkali-activated cement paste, mortar, and concrete. Constr Build Mater 186:191–206. https://doi.org/10.1016/J.CONBUILDMAT.2018.07.119

21. Jang JG, Park SM, Lee HK (2016) Physical barrier effect of geopolymeric waste form on diffusivity of cesium and strontium. J Hazard Mater 318:339–346. https://doi.org/10.1016/j.jhazmat.2016.07.003

22. Bondar D, Ma Q, Soutsos M, et al (2018) Alkali activated slag concretes designed for a desired slump, strength and chloride diffusivity. Constr Build Mater 190:191–199. https://doi.org/10.1016/j.conbuildmat.2018.09.124

23. Bernal SA, Mejía De Gutiérrez R, Provis JL (2012) Engineering and durability properties of concretes based on alkali-activated granulated blast furnace slag/metakaolin blends. Constr Build Mater 33:99–108. https://doi.org/10.1016/j.conbuildmat.2012.01.017

24. Lloyd RR, Provis JL, Van Deventer JSJ (2010) Pore solution composition and alkali diffusion in inorganic polymer cement. Cem Concr Res 40:1386–1392. https://doi.org/10.1016/j.cemconres.2010.04.008

25. Kuenzel C, Cisneros JF, Neville TP, et al (2015) Encapsulation of Cs/Sr contaminated clinoptilolite in geopolymers produced from metakaolin. J Nucl Mater 466:94–99. https://doi.org/10.1016/j.jnucmat.2015.07.034

26. Arbel Haddad M, Ofer-Rozovsky E, Bar-Nes G, et al (2017) Formation of zeolites in metakaolin-based geopolymers and their potential application for Cs immobilization. J Nucl Mater 493:168–179. https://doi.org/10.1016/j.jnucmat.2017.05.046

27. Arbel Haddad M, Ofer-Rozovsky E, Bar-Nes G, et al (2017) Formation of zeolites in metakaolin-based geopolymers and their potential application for Cs immobilization. J Nucl Mater 493:168–179. https://doi.org/10.1016/j.jnucmat.2017.05.046

28. Berger S, F. Frizon, Fournel V, Cau-dit-Coumes C (2007) Immobilization of Cesium in Geopolymeric Matrix: a formulation study. 12th Int Congr Chem Cem 1–11

29. Amorim Júnior NS, Andrade Neto JS, Santana HA, et al (2021) Durability and service life analysis of metakaolin-based geopolymer concretes with respect to chloride penetration using chloride migration test and corrosion potential. Constr Build Mater 287:. https://doi.org/10.1016/j.conbuildmat.2021.122970

30. Noushini A, Nguyen QD, Castel A (2021) Assessing alkali-activated concrete performance in chloride environments using NT Build 492. Mater Struct Constr 54:1–15. https://doi.org/10.1617/s11527-021-01652-7

31. Gluth GJG, Arbi K, Bernal SA, et al (2020) RILEM TC 247-DTA round robin test: carbonation and chloride penetration testing of alkali-activated concretes. Mater Struct Constr 53:1–17. https://doi.org/10.1617/s11527-020-1449-3

32. Fu C, Ye H, Zhu K, et al (2020) Alkali cation effects on chloride binding of alkali-activated fly ash and metakaolin geopolymers. Cem Concr Compos 114:103721. https://doi.org/10.1016/j.cemconcomp.2020.103721

33. Benavent V, Steins P, Sobrados I, et al (2016) Impact of aluminum on the structure of geopolymers from the early stages to consolidated material. Cem Concr Res 90:27–35. https://doi.org/10.1016/j.cemconres.2016.09.009

34. Mortlock RF, Bell AT, Radke CJ (1991) NMR investigations of tetrapropylammonium aluminosilicate and borosilicate solutions. J Phys Chem 95:372–378. https://doi.org/10.1021/j100154a067

35. Massiot D, Fayon F, Capron M, et al (2002) Modelling one- and two-dimensional solid-state NMR spectra. Magn Reson Chem 40:70–76. https://doi.org/10.1002/mrc.984

36. Duxson P, Lukey GC, van Deventer JSJ (2006) Thermal evolution of metakaolin geopolymers: Part 1 - Physical evolution. J Non Cryst Solids 352:5541–5555. https://doi.org/10.1016/j.jnoncrysol.2006.09.019

37. Tian Q, Nakama S, Sasaki K (2019) Immobilization of cesium in fly ash-silica fume based geopolymers with different Si/Al molar ratios. Sci Total Environ 687:1127–1137. https://doi.org/10.1016/j.scitotenv.2019.06.095

38. Muller ACA, Scrivener KL, Gajewicz AM, McDonald PJ (2013) Use of bench-top NMR to measure the density, composition and desorption isotherm of C-S-H in cement paste. Microporous Mesoporous Mater 178:99–103. https://doi.org/10.1016/j.micromeso.2013.01.032

39. Scrivener K, Snellings R, Lothenbach B (2016) A Practical Guide to Microstructural Analysis of Cementitious Materials

40. Kurumisawa K, Jensen OM (2020) Thermoporometry and proton NMR measurement on cement paste equilibrated at different relative humidities. J Adv Concr Technol 18:. https://doi.org/10.3151/jact.18.456

41. Kurumisawa K (2015) Application of thermoporometry for evaluation of properties of hardened cement paste. Constr Build Mater 101:926–931. https://doi.org/10.1016/j.conbuildmat.2015.10.061

42. Hou D, Zhang J, Pan W, et al (2020) Nanoscale mechanism of ions immobilized by the geopolymer: A molecular dynamics study. J Nucl Mater 528:151841. https://doi.org/10.1016/j.jnucmat.2019.151841

43. Nokken M, Boddy A, Hooton RD, Thomas MDA (2006) Time dependent diffusion in concrete-three laboratory studies. Cem Concr Res 36:200–207. https://doi.org/10.1016/j.cemconres.2004.03.030

44. Luping T, Gulikers J (2007) On the mathematics of time-dependent apparent chloride diffusion coefficient in concrete. Cem Concr Res 37:589–595. https://doi.org/10.1016/j.cemconres.2007.01.006

45. Jaya NA, Yun-Ming L, Cheng-Yong H, et al (2020) Correlation between pore structure, compressive strength and thermal conductivity of porous metakaolin geopolymer. Constr Build Mater 247:118641. https://doi.org/10.1016/j.conbuildmat.2020.118641

46. Kubba Z, Fahim Huseien G, Sam ARM, et al (2018) Impact of curing temperatures and alkaline activators on compressive strength and porosity of ternary blended geopolymer mortars. Case Stud Constr Mater 9:e00205. https://doi.org/10.1016/j.cscm.2018.e00205

47. Lippmaa E, Mági M, Samoson A, et al (1981) Investigation of the Structure of Zeolites by Solid-State High-Resolution 29Si NMR Spectroscopy. J Am Chem Soc 103:4992–4996. https://doi.org/10.1021/ja00407a002

48. Brun M, Lallemand A, Quinson J-F, Eyraud C (1977) A new method for the simultaneous determination of the size and shape of pores: the thermoporometry. Thermochim Acta 21:59–88. https://doi.org/10.1016/0040-6031(77)85122-8

49. Snyder KA, Bentz DP (2004) Suspended hydration and loss of freezable water in cement pastes exposed to 90% relative humidity. Cem Concr Res 34:2045–2056. https://doi.org/10.1016/j.cemconres.2004.03.007

50. Kurumisawa K, Mami Ojima (2020) Physical properties and Microstructure of metakaolin based geopolymer. In: Proceedings of the ConMat'20, Advances in Construction Materials. Fukuoka, pp 413–422

51. Bentz DP, Snyder KA, Cass LC, Peltz MA (2008) Doubling the service life of concrete structures. I: Reducing ion mobility using nanoscale viscosity modifiers. Cem Concr Compos 30:674–678. https://doi.org/10.1016/j.cemconcomp.2008.05.001

Table 1. Chemical composition of MK (mass%)

Na_2O	Al_2O_3	SiO_2	K_2O	CaO	TiO_2	Fe_2O_3
0.64	45.21	52.48	0.12	0.02	1.62	0.34

Table 2. Alkali activator compositions

Sample	Alkali activator(mol/mol)			
	M_2O	M_2O/Al_2O_3	SiO_2/Al_2O_3	H_2O/Al_2O_3
K11	K_2O	1.0	1.0	11.0
K9	K_2O			9.0
0.66K	K_2O		1.5	11.0
N11	Na_2O		1.0	
KN11	$0.5K_2O+0.5Na_2O$			

Table 3. Si NMR results of alkali activator

	K11	K9	0.66K	N11	KN11
Q^0	20.9	22.9	7.25	28.8	25.9
Q^1	29.2	32.7	22.0	34.1	32.1
$Q^{2\Delta}$	20.4	18.5	18.0	21.0	20.4
Q^2	17.2	16.0	28.4	10.5	14.1
$Q^{3\Delta}$	6.7	6.4	10.4	4.1	5.3
Q^3	5.6	3.7	14.1	1.6	2.2

Figure 1. Compressive strengths and UPVs of the geopolymers

Figure 2. Apparent diffusion coefficients of cesium ions in the geopolymers

Figure 3 (a) Cesium adsorption isotherms of the geopolymers, (b) Maximum saturation capacities of the geopolymers

Figure 4. Maximum saturation capacities and apparent diffusion coefficients of cesium ions in the geopolymers

Figure 5. Pore volume measured by MIP and N_2 adsorption, and BET surface areas, as determined from nitrogen adsorption measurements, of the geopolymers

Figure 6. Pore size distribution of the geopolymers, as determined by MIP

Figure 7 (a) Pore volume measured by MIP and N_2 adsorption, and compressive strength of the geopolymers, (b) Pore volume measured by MIP and N_2 adsorption, and apparent diffusion coefficients of cesium ions in the geopolymers, (c) BET surface area and apparent diffusion coefficients of cesium ions in the geopolymers

Figure 8 (a) ^{27}Al NMR results for the geopolymers, (b) ^{29}Si DD MAS NMR results for the geopolymers

Figure 9 (a) LT-DSC result for the geopolymers during the freezing process, (b) LT-DSC result for the geopolymers during the melting process

Figure 10 (a) Proton NMR results for the geopolymers, (b) Normalized Proton NMR results for the geopolymers

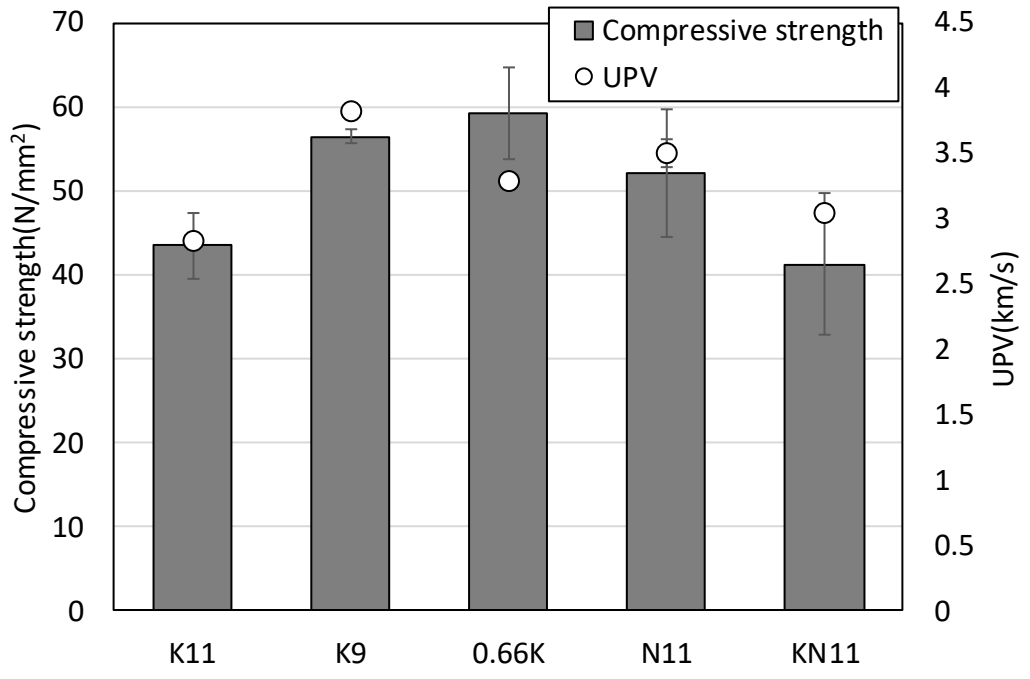

Figure 1

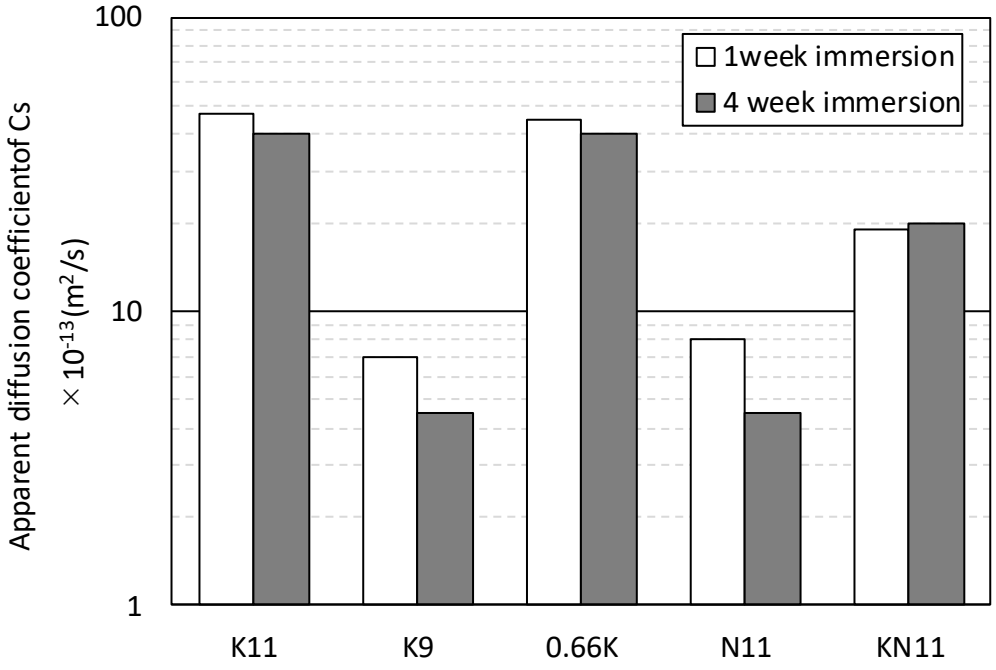

Figure 2

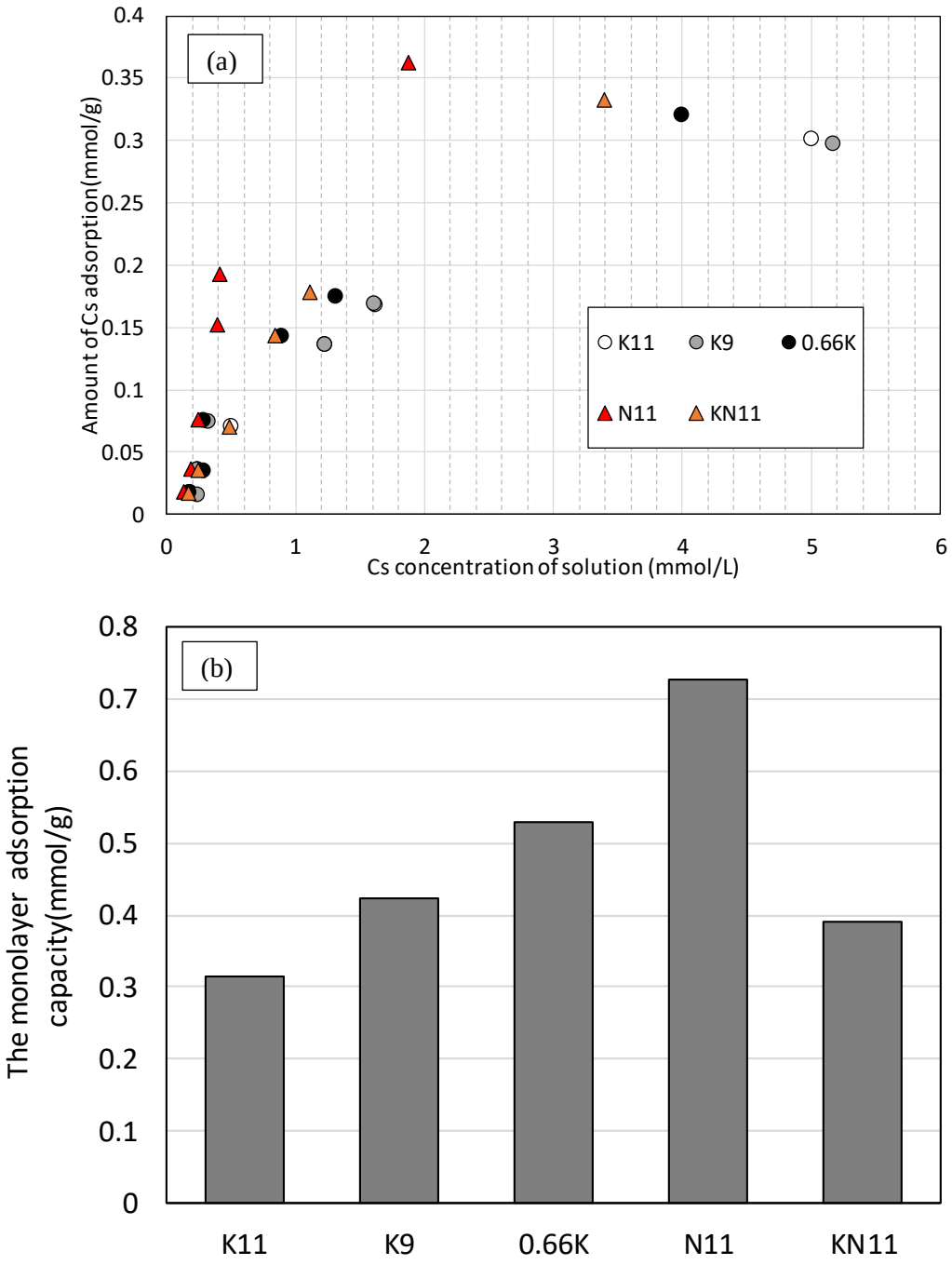
(a)
Amount of Cs adsorption (mmol/g)
Cs concentration of solution (mmol/L)
K11
K9
0.66K
N11
KN11
0
0.05
0.1
0.15
0.2
0.25
0.3
0.35
0.4
0
1
2
3
4
5
6
(b)
The monolayer adsorption capacity(mmol/g)
0
0.1
0.2
0.3
0.4
0.5
0.6
0.7
0.8
K11
K9
0.66K
N11
KN11

Figure 3

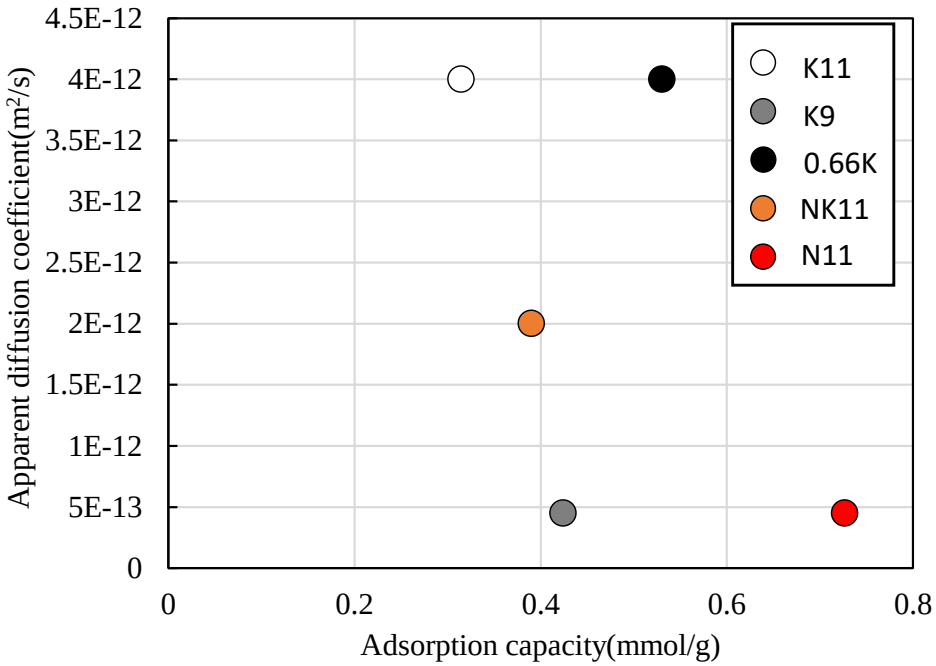

Figure 4

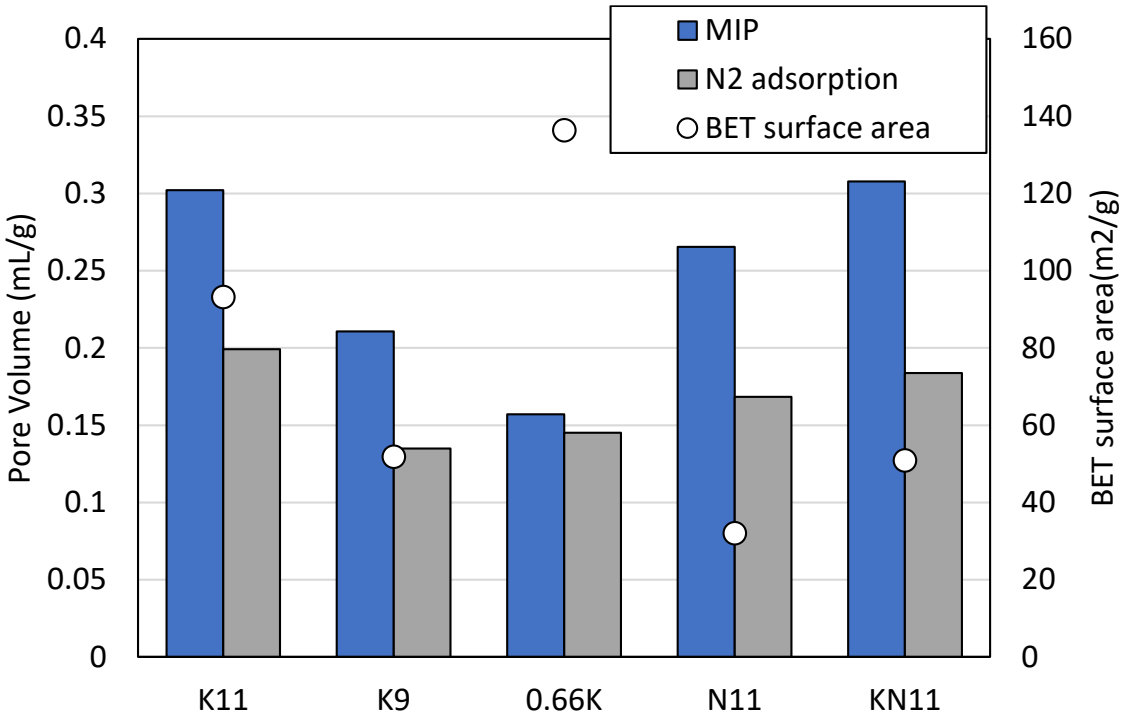

Figure 5

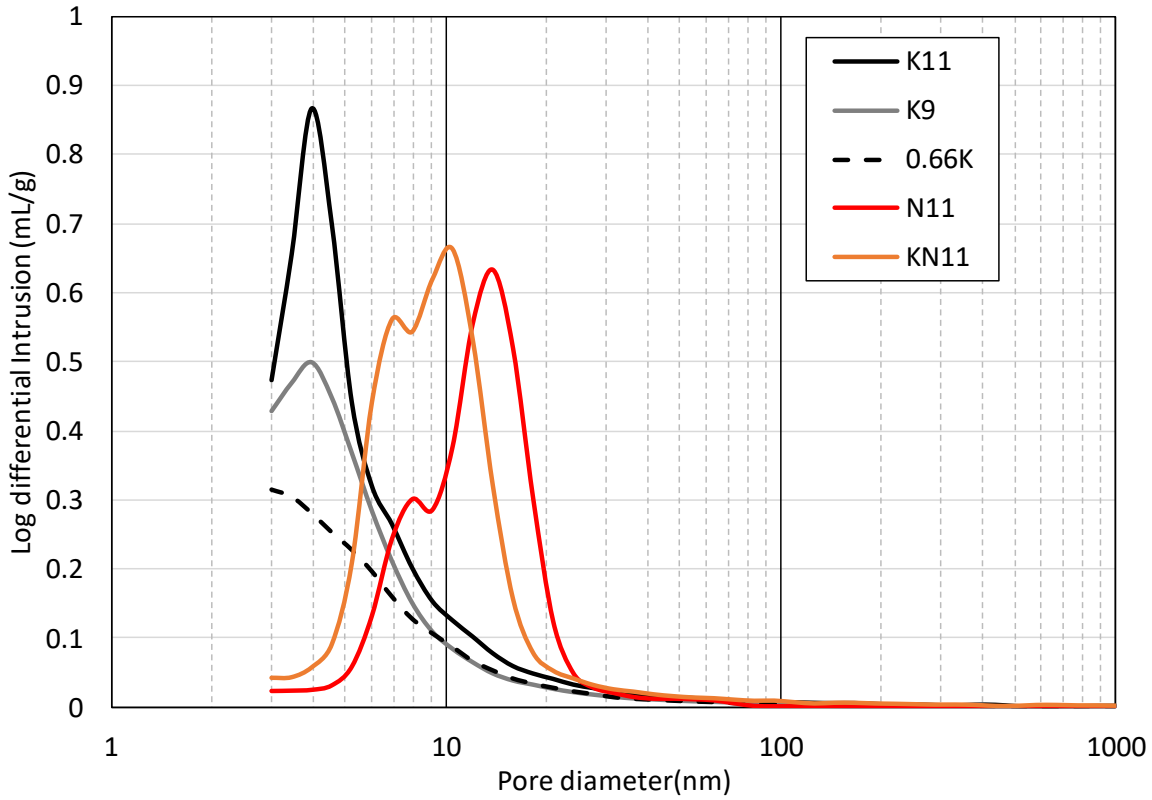
Log differential Intrusion (mL/g)
1
0.9
0.8
0.7
0.6
0.5
0.4
0.3
0.2
0.1
0
1
10
100
1000
Pore diameter(nm)
K11
K9
0.66K
N11
KN11

Figure 6

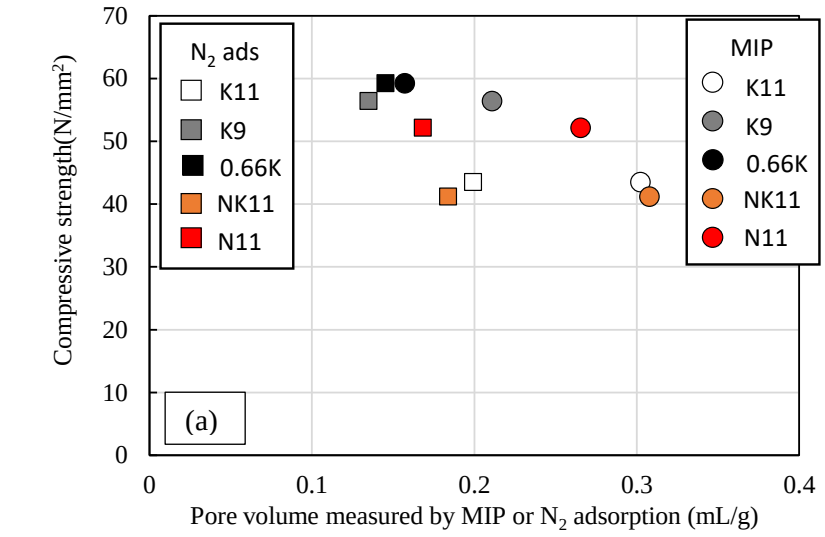
Compressive strength(N/mm²)
70
60
50
40
30
20
10
0
0
0.1
0.2
0.3
0.4
Pore volume measured by MIP or N2 adsorption (mL/g)
N2 ads
K11
K9
0.66K
NK11
N11
MIP
K11
K9
0.66K
NK11
N11
(a)

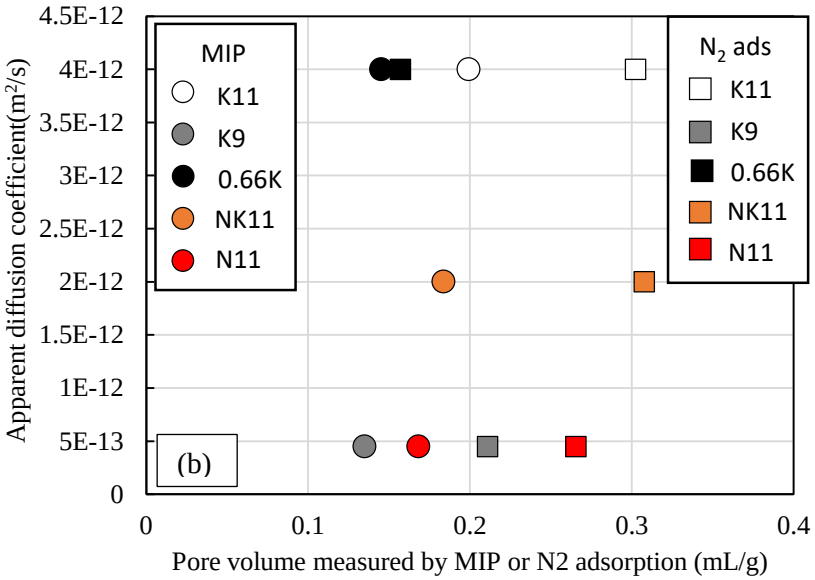
Apparent diffusion coefficient(m²/s)
4.5E-12
4E-12
3.5E-12
3E-12
2.5E-12
2E-12
1.5E-12
1E-12
5E-13
0
0
0.1
0.2
0.3
0.4
Pore volume measured by MIP or N2 adsorption (mL/g)
MIP
K11
K9
0.66K
NK11
N11
N2 ads
K11
K9
0.66K
NK11
N11
(b)

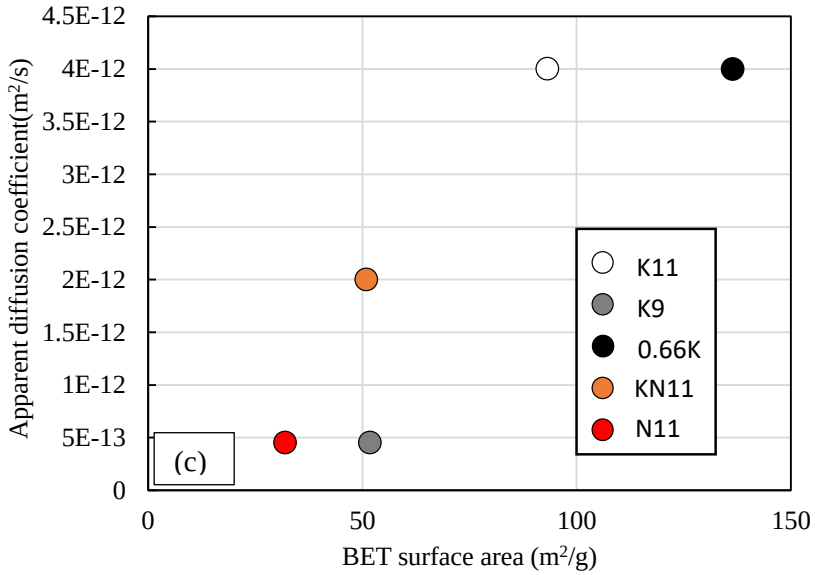
Apparent diffusion coefficient(m²/s)
4.5E-12
4E-12
3.5E-12
3E-12
2.5E-12
2E-12
1.5E-12
1E-12
5E-13
0
0
50
100
150
BET surface area (m²/g)
K11
K9
0.66K
KN11
N11
(c)

Figure 7

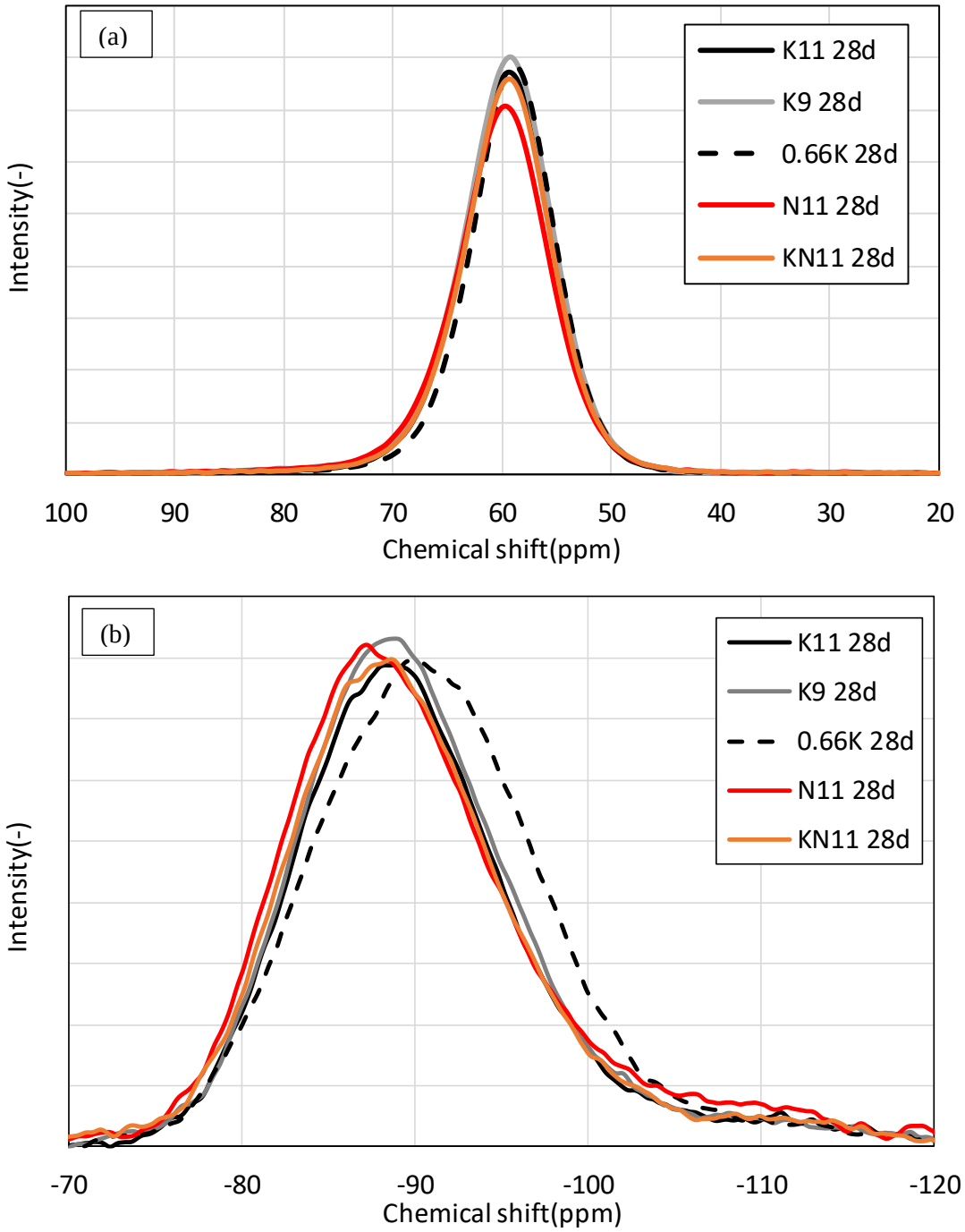
(a)
K11 28d
K9 28d
0.66K 28d
N11 28d
KN11 28d
Intensity(-)
100
90
80
70
60
50
40
30
20
Chemical shift(ppm)
(b)
K11 28d
K9 28d
0.66K 28d
N11 28d
KN11 28d
Intensity(-)
-70
-80
-90
-100
-110
-120
Chemical shift(ppm)

Figure 8

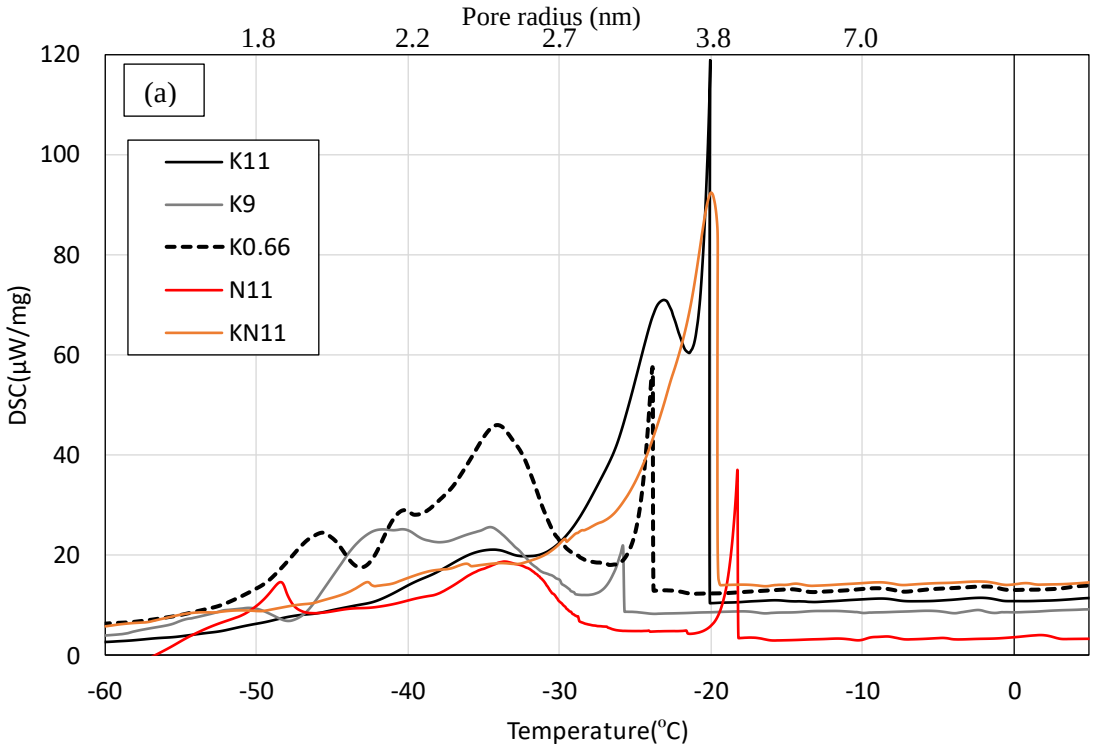
Pore radius (nm)
1.8
2.2
2.7
3.8
7.0
(a)
K11
K9
K0.66
N11
KN11
DSC(μW/mg)
120
100
80
60
40
20
0
-60
-50
-40
-30
-20
-10
0
Temperature(°C)

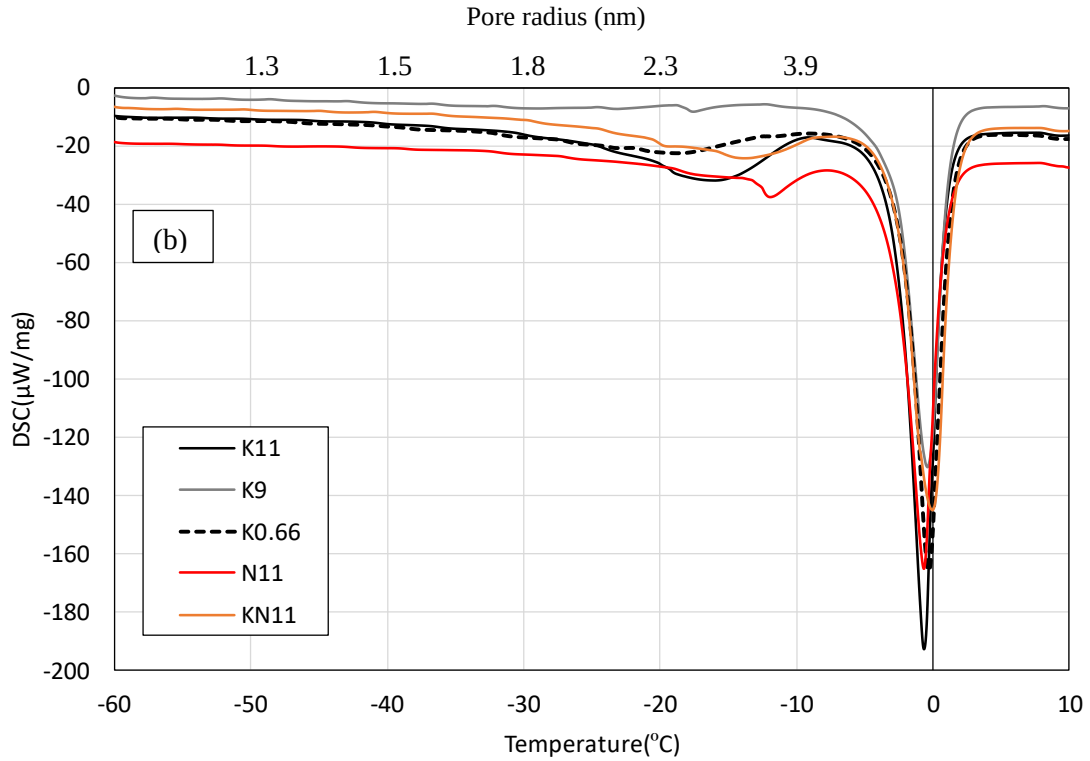
Pore radius (nm)
1.3
1.5
1.8
2.3
3.9
(b)
K11
K9
K0.66
N11
KN11
DSC(μW/mg)
0
-20
-40
-60
-80
-100
-120
-140
-160
-180
-200
-60
-50
-40
-30
-20
-10
0
10
Temperature(°C)

Figure 9

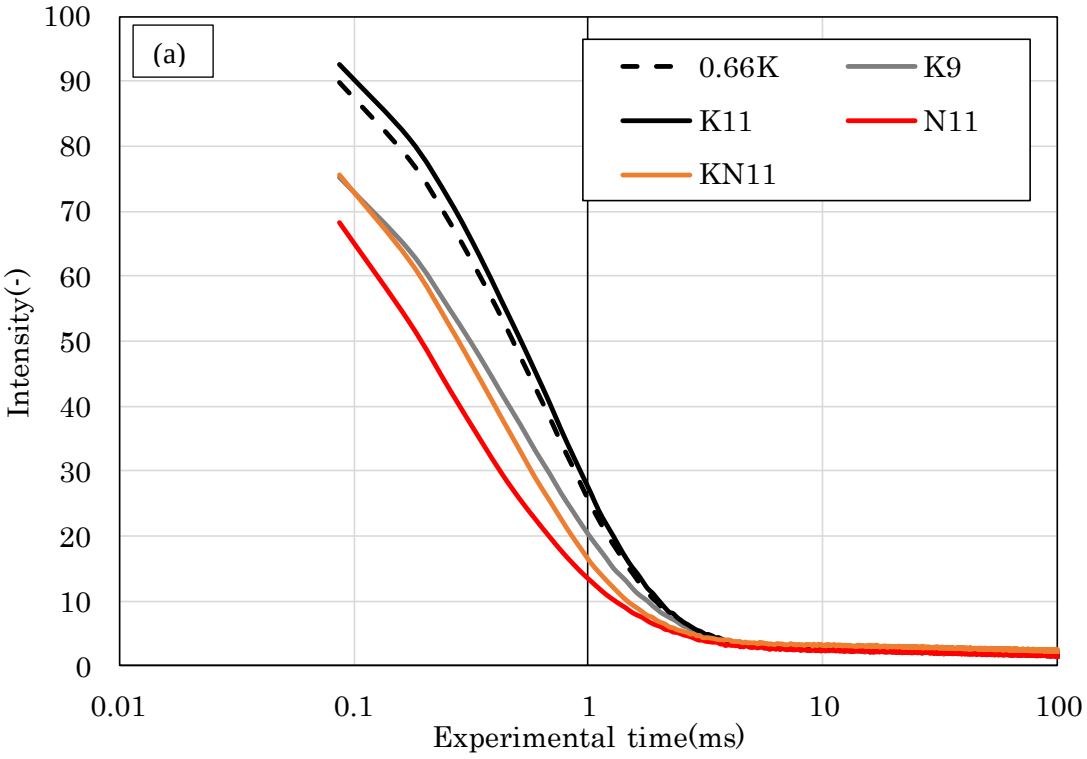
(a)
0.66K
K9
K11
N11
KN11
Intensity(-)
100
90
80
70
60
50
40
30
20
10
0
0.01
0.1
1
10
100
Experimental time(ms)

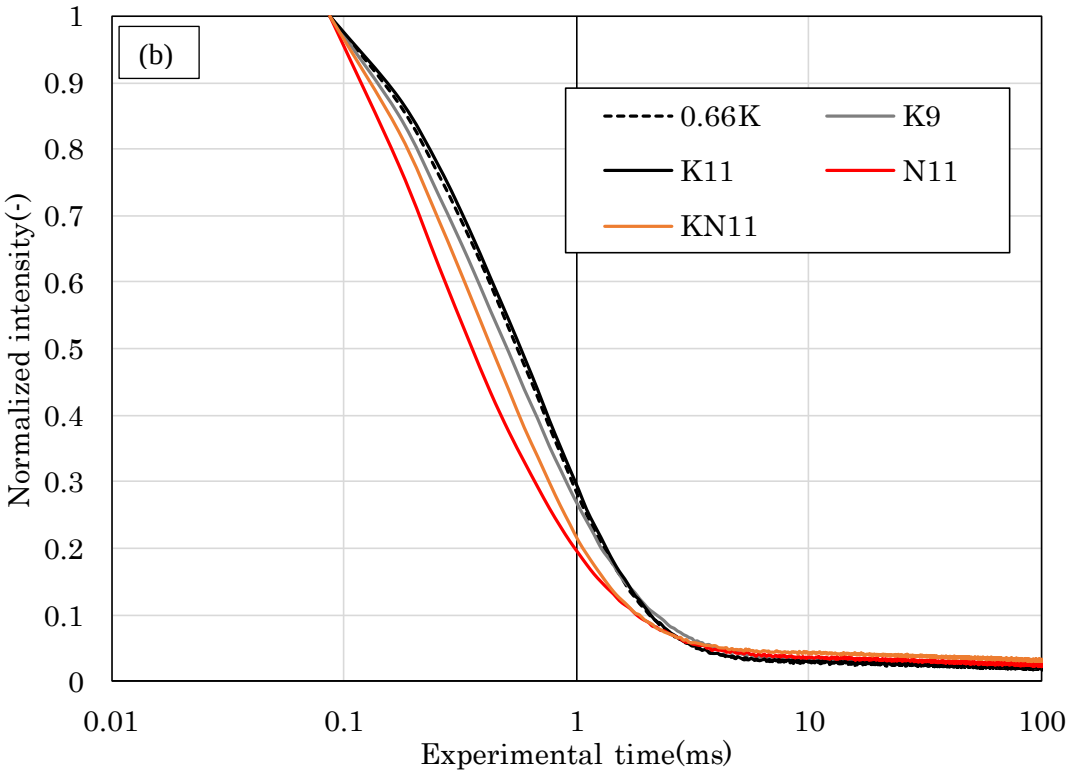
(b)
0.66K
K9
K11
N11
KN11
Normalized intensity(-)
1
0.9
0.8
0.7
0.6
0.5
0.4
0.3
0.2
0.1
0
0.01
0.1
1
10
100
Experimental time(ms)

Figure 10